Unraveling the mechanisms of room-temperature catalytic degradation of indoor formaldehyde and the biocompatibility on colloidal TiO_2-supported MnO_x–CeO_2†

Haiwei Li,[a] Tingting Huang,[b] Yanfeng Lu,[b] Long Cui,[a] Zhenyu Wang,[bc] Chaofeng Zhang[b], Shuncheng Lee,[a *] Yu Huang,[b*] Junji Cao,[bc] and Wingkei Ho[d]

[a]*Department of Civil and Environmental Engineering, The Hong Kong Polytechnic University, Hung Hom, Hong Kong*
[b]*Key Lab of Aerosol Chemistry & Physics, Institute of Earth Environment, Chinese Academy of Sciences, Xi'an 710061, China*
[c]*School of Human Settlements and Civil Engineering, Xi'an Jiaotong University, Xi'an 710049, China*
[d]*Department of Science and Environmental Studies, The Education University of Hong Kong, Hong Kong*

Abstract

This work overcomes the limits in room-temperature and moisture-dependent activity by transition-metal oxide-based catalysts for sub-ppm formaldehyde removal. The active-site exposure and self-assembly hydrophilicity were highlighted in MnO_x–CeO_2 (MCO) nanospheres after loading of colloidal 2.1 wt. % TiO_2 particles (TO–MCO). Approximately 57 % (relative humidity = 72 %) and 41 % (dry air) of recycling catalytic activity at 35 °C were achieved. Our results proved that surface electron transfer, which was previously weakened because of the loss of surface oxygen species and unsuitable defect-site depositions of low active ions, in MCO catalyst was recovered by the dispersion of hydrophilic Ti–O groups. This electron transfer was also strongly correlated with the specific surface area, porosity, and oxidation states of transition-metals. The greater active-site exposure derived from the cyclic electron transfer eventually enhanced the HCHO chemisorption and participation of oxygen species on the surface of TO–MCO throughout the bimetallic (Mn–Ce) dismutation reactions. Abundant superoxide radicals that were activated from these oxygen species prompted a nucleophilic attack on carbonyl bonds. Direct photoionization mass spectrometry determined the formic acid, minor dioxirane, and faint $HOCH_2OOH$ as intermediates of the HCHO selectivity to CO_2. The cytotoxicity of catalyst-exposed to yeast cells was evaluated for the potential environment-friendly application in indoors.

1. Introduction

Long-term exposure to indoor formaldehyde (HCHO) can cause severe irritation of the eye, skin, and upper respiratory tract, and even pose cancer risks to humans. [1-3] Among volatile organic compounds, HCHO has the simplest molecular structure but is extremely prone to desorb or escape into indoor environments at increased temperatures. Conventional processes like physical adsorption and photocatalysis inevitably incur secondary pollution.[4, 5] For instance, on the catalyst surface, the desorption of adsorbed HCHO induced by thermal disturbance from light irradiation during the photocatalytic process can reduce the removal efficiencies and ultimately restrict its practical application [6, 7].

Room-temperature catalytic degradation (RCD) is currently regarded as a promising strategy to remove ppm-level HCHO [7-10]. The wide application of supported noble metallic catalysts (containing Au, Ag, Pt, and Pd) is restricted by their high cost and demanding control of sizes and shapes [9, 11, 12], although the reported activity approximated above 90% at 25–110 °C [13-17]. In contrast, fabricating non-noble metallic nanocomposites of representative transition-metal catalysts with conductive capacitor materials (e.g. Mn–Ce [18-20], Mn–Co [21, 22], Mn–Fe [23, 24], Mn–Ce–Zr [25, 26], Mn–Ce–Al [27, 28]) is of great importance in the enhancement of bimetallic dismutation reactions, ranging 70–95 % at 70–210 °C. By far, it is of great necessity and interest to develop a kind of more efficient catalyst for indoor sub-ppm HCHO removal at (near) room temperature.

Owing to its high thermal resistance and structural flexibility, manganese oxide (MnO_x), often modified by other catalysts or elements, is extensively used as a sorbent and substrate in hybrid fabrication [9, 29-31]. An ensuing redox loop of the oxidation states of manganese ions functionalizes MnO_x with reversible electron transfer and rapid cation diffusion [31, 32]. Surface active-site exposure of pristine MnO_x can be enhanced by this electron transfer under the higher charge–discharge rates when its reduced-valence ions durably capture free electrons from electrode materials with high conductivity (e.g. CeO_2 [33-35], Co_3O_4 [36], and Fe_3O_4 [37]) at low temperatures. Among them, MnO_x–CeO_2 has been frequently reported to exhibit the comparatively high redox activities [18, 38]. As similar with most of catalysts, however, the activity of MnO_x–CeO_2 is greatly affected with a sharp drop of react temperature to the ambient. In addition, oxygen-vacancy sites are formed via the entry of manganese ions into ceria and the surface adsorption active-sites are reduced because of the loss in oxygen species. Low-frequency recycling adsorption and catalysis are further deteriorated by the unsuitable depositions of low active ions and/or other redundant ions on the oxygen-vacancy sites of MnO_x–CeO_2. [31, 39]

Furthermore, moisture is helpful in HCHO adsorption and transfer of oxygen species on the transition-metal catalysts for activation of reactive radicals. In fact, practical activities lag behind laboratory estimates due to temporal or regional variations in the atmospheric moisture [8, 21]. Therefore, colloidal TiO_2 that has particularly flexible structure in thin-loading synthesis is introduced to gain the self-hydrophilic property

[40, 41] and oxygen-defect remediation of MnO_x–CeO_2 [39]. In literature, potential effects of active-site chemisorption and activation of reactive oxygen species, which are induced by the cyclic surface electron transfer, are underestimated in RCD mechanisms [8, 21, 31]. Associated with the HCHO selection to CO_2, an in-depth insight into types and lifespans of possible trace-level formate intermediates and by-products can be continuously investigated by the high resolution photoionization mass spectra under the ambient pressure and temperature [42, 43], leading to verify the practical implications in the perspective of stability, deactivation mechanisms, and surficial aging accumulated compounds.

Here, targeting for better performance on RCD activity of sub-ppm HCHO removal, TiO_2-supported MnO_x–CeO_2 (TO–MCO) was obtained via a consecutive hydrothermal and colloidal reflux-condensation method and was systematically characterized. TO–MCO exhibited distinct crystalline structure and morphology with those of pristine MnO_x–CeO_2. The generated hydrophilic –OH/TiO_2 interfacial structure [40] enhanced HCHO preadsorption under low-moisture conditions as well as surface cyclic electron transfer via the remediation of the oxygen defects on MnO_x–CeO_2 surfaces. The role of the interactions of each element in chemisorption and superoxide radical activation induced by the electron transfer was identified. Investigations on the recycling activity for ppb-level HCHO removal were then carried out at room temperature. Aside from *in situ* C 1s XPS and *in situ* DRIFT studies, molecular-level conversion pathways during the catalytic process were probed by direct photoionization mass spectrometry. Overall reactivity pathways and mechanisms were proposed accordingly. The results of toxicity assessment authenticated benign biocompatibility of TO–MCO.

2. Experimental Section

2.1 Catalyst synthesis

The preparation of colloidal TiO_2-supported MnO_x–CeO_2 catalyst followed a consecutive hydrothermal and colloidal reflux-condensation route. (i) $Mn(NO_3)_2$ (50 vol. % 0.008 M) and $Ce(NO_3)_3{\cdot}6H_2O$ (0.008 M) were dissolved in 20 mL of deionized water (18 MΩ) stoichiometrically added with $(NH_4)_2S_2O_8$ (0.016 M) to form a soluble solution. The resulting solution was stirred for 2 h, transferred into a 50 mL Teflon-lined stainless steel, and autoclaved at 190 °C for 12 h. (ii) The hydrothermal product, MnO_x–CeO_2 (MCO), was washed and centrifuged with ultrapure water from three to five times before drying at 70 °C and calcinating for 6 h at 350 °C. (iii) The final product, TO–MCO, was harvested by gradually mixing MCO with 0.12 M TiO_2 collosol (Fig. S1) by reflux condensing in a thermostatic water bath at 60 °C with stirring for over 4 h.

2.2. Characterizations

To determine the crystal properties, powder X-ray diffraction (XRD) was performed with a Philips X'pert Pro Super diffractometer using Cu Kα (λ = 0.15406 nm) radiation at a scan rate of 0.017° in the 2θ range of 10°–80°. The micromorphology of the samples was illustrated by a SUPRA 55 field-emission scanning electron microscope and a JEOL JEM–2010 transmission electron microscope. The Brunauer–Emmett–Teller (BET) surface area was measured by N_2 adsorption/desorption isotherms at –196.15 °C on a Micrometrics Gemini VII 2390 instrument. Thermogravimetric (TG) studies were conducted on a Setaram Setsys 16/18 thermoanalyzer at a heating rate of 10 $K{\cdot}min^{-1}$ in N_2 atmosphere. X-ray photoemission spectroscopy (XPS) for chemical compositions was recorded on a Thermo ESCALAB 250 system, wherein all the binding energies were calibrated to the C 1s peak at 284.8 eV of the surface adventitious carbon.

Temperature-programmed reduction (H_2-TPR) and temperature-programmed desorption (TPD) were performed using a thermal conductivity detector. The experiments were performed in a quartz reactor. Approximately 50 mg of as-prepared samples was pretreated first with 30 $mL{\cdot}min^{-1}$ of pure N_2 at 300 °C for 100 min and then adsorbed with 500 ppb NH_3 for 30 min after cooling down to room temperature. Physically adsorbed NH_3 was purged out with 30 $mL{\cdot}min^{-1}$ of pure helium (He) gas for 60 min at 150 °C. H_2-TPR was then heated to 800 °C with 10 $°C{\cdot}min^{-1}$ rate using a mixture of 10% H_2 in argon (Ar) gas after purging pretreatment at 300 °C with 10% H_2/Ar for 60 min. NH_3-TPD experiments were finally performed at 650 °C and heating rate of 10 $°C{\cdot}min^{-1}$ in a pure He atmosphere. *In situ* electron spin resonance (ESR) signals were recorded on a Bruker ER200–SRC spectrometer at –143.15 °C. *In situ* XPS measurements calibrated via 284.5 eV of adventitious carbon (C_A) and 288.5 eV of formate species and/or HCHO (C_F) were investigated using a Vacuum Generators Escalab 220 XL spectrometer with Al Kα X-rays (hν = 1486.6 eV) irradiation. After HCHO-saturated samples were pretreated under Ar feed gas at an increasing rate of 2 $°C{\cdot}min^{-1}$ to the as-required test temperature, the samples were cooled to 25 °C under Ar and then analyzed in a catalytic cell of the XPS analyzer. *In situ* diffuse reflectance infrared Fourier transform (*in situ* DRIFT) spectrometry was recorded on a Fourier transform infrared spectrometer (VERTEX 70, Bruker) with an *in situ* cell reactor. The spectra were recorded with a resolution of 4 cm^{-1} (32 scans). After purging all the samples with He gas at 300 °C until the calibration of the background spectrum was completed, 50 ppm of initial HCHO concentration was then injected into the cell at a flow rate of 30 $mL{\cdot}min^{-1}$ via mass flow controllers. Pressured oxygen was used as the balance gas.

2.3. Catalytic activity measurement

HCHO catalytic oxidation was performed in a thermostatic fixed-bed reaction system, consisting of three main sections, namely, mass flow controller, thermostatic fixed-bed reactor, and real-time analytical system. Gaseous HCHO was diluted by the carrier gas (21 vol. % O_2 balanced by N_2, pristine RH = 0.7 %) and the relative humidity (RH = 50 %, 72 %, and 90 %) was adjusted by changing the ratio of humid air in the carrier gas. Up to 100 $mL{\cdot}min^{-1}$ of the flowrate and 500 ppb of inlet HCHO were stoichiometrically determined by the mass flow controller (Brooks 5860E) and the corresponding GHSV was 12,000 h^{-1}. Approximately 150 mg test catalysts sieved between 40 and 60 mesh were loaded on silica wool in a stainless-steel thermocouple tube (8 mm diameter) of the thermostatic fixed-bed reactor. The operating temperature was

automatically controlled with T-measuring thermocouples inside of the stainless-steel tube. The outlet concentration of HCHO from the reactor was monitored by a photoacoustic gas monitor (Innova 1412i, Denmark) with detection limit of 0.04 ppm. The C_t and C_0 are the concentration of HCHO at an initial and any given time, respectively. Since a challenge in measurements of sub-ppm HCHO conversion CO_2, the final CO_2 was sampled and accumulated into a 25 L Teflon airbag in a cumulative run of 30 min or above, and then can be detected by the photoacoustic monitor (UA0983 optical filter with CO_2 detection limit of 5 ppm), namely the cumulative HCHO conversion to CO_2. Recycling catalytic activity was carried out in 5 batch modes of 36-minute measurements, each of which continued when the HCHO concentration was back to its initial level.

3. Results and Discussion

3.1. Optimal crystal structures and morphology

The crystalline phases were compared with the precursors of TO–MCO sample through XRD (Fig. 1a). Compared with pristine MnO_2 (JCPDS No. 24–735) and CeO_2 (JCPDS No. 89-8436), no characteristic peak related to pure ceria was observed and the 2θ for the (111) diffraction peak remarkably shifted to low angles for MnO_x–CeO_2. This shift was mainly due to the formation of as-anticipated MnO_x–CeO_2 catalyst, in which some Ce^{4+} ions (0.094 nm) of CeO_2 interlayer were replaced by manganese ions Mn^{n+} (Mn^{4+} 0.054 nm and Mn^{3+} 0.066 nm). Although some faint XRD characteristic peaks of spherical MnO_x–CeO_2 for TO–MCO were distorted by asymmetric dispersions of TiO_2 particles on the surfaces of MCO, the (111) orientation was identified (d111 = 0.489 nm) for MnO_x–CeO_2 and also observed at the interface between TiO_2 and MCO for TO–MCO. The negative shift of the diffraction pattern was estimated to the sharp and intense peak (111) (2θ = 25.35°), which was slightly broadened by the TiO_2 (101) diffraction peak (Fig. S1). The other diffraction peaks were indexed to the anatase phase of TiO_2 [e.g. (103) at 37.00° and (211) at 55.15°] [44]. Therefore, the well-desired dispersion of colloidal TiO_2 on the surface of MCO was successfully obtained, implying that TO–MCO was of nanoparticle size and high purity. The chemical compositions of the as-prepared TO–MCO were examined by a comparative study of laboratorial HCHO conversion (Fig. S2) and turnover number (TON) with respect to catalytic contents (Table S1). The optimal Mn/(Mn+Ce) molar ratio was 0.38:1, and approximately 2.1 wt. % loading of colloidal TiO_2 was finalized.

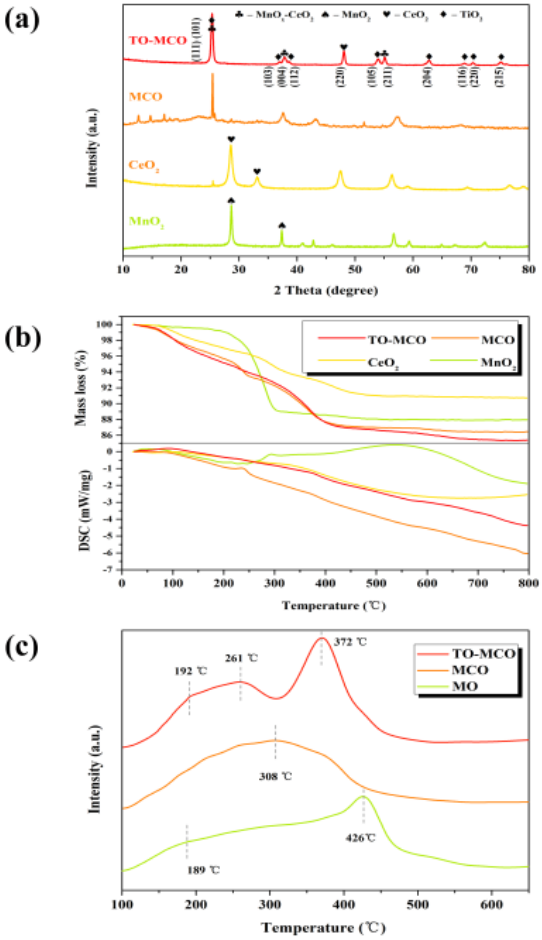

Fig. 1 XRD patterns of MnO_2, CeO_2, MCO, and TO–MCO catalyst (a); thermogravimetry differential scanning calorimetry profiles of the as-prepared catalysts (b); H_2-TPR profiles of the as-prepared catalysts (c).

Both MCO and TO–MCO presented strong thermal stability and showed three various stages of weight loss, as indicated by the TG analysis results (Fig. 1b). In the first stage, surface-adsorbed water was lost before the temperature reached 250 °C. The second stage started at 300–450 °C, during which the amount of lattice oxygen started to decline, and Mn^{4+} was reduced to Mn^{3+}. The third stage started at 550–650 °C, wherein the amount of lattice oxygen continued to decrease. The presumptions of the multistage generation of lattice oxygen remained consistent with a previous study [29]. Notably, the comparatively higher loss was ascribed to the decrease of lattice oxygen for TO–MCO more than MCO under the third stage, reflecting that oxygen vacancies of MCO surfaces were remediated after the loading of TiO_2.

The redox potentials of the as-prepared catalysts were investigated by H_2-TPR measurements. Compared with bare MnO_2, a shift to lower temperatures increase of intensity of the reduction peaks were ascribed by the Ce reduction along with reduction of manganese ions for Ce-contained MnO_x–CeO_2 [28]. The profiles of the TO–MCO sample (Fig. 1c) revealed three reduction peaks at a broad temperature ranging from 150 °C to 450 °C. The existence of mixed-valence MnO_2–Mn_2O_3 and Mn^{4+}–O–Ce^{4+} as active center in the catalysts can improve the redox properties of manganese oxides and corresponds with the XPS investigations (Fig. S3), while colloidal TiO_2 barely attended in the dismutation reactions due to its loaded-mass control (Table S1) and distinct crystalline structure (also see in Fig. 2b). Compared with MCO which presented an apparent maximum at 308 °C in the overlapping peaks, the reduction process at lower temperature for TO–MCO was ascribed to the enhanced mobility of oxygen species [18, 45] and generation of –OH species [8] at around 192 °C. The reduction of Mn^{3+} into Mn^{4+} can be assigned at a low-temperature reduction peak and continuous reduction of Mn^{4+} into Mn^{2+} [18]. Mn^{2+} did not appear in the dismutation reactions (in Fig. S3b). Hence, the increased contribution of high-temperature peak to the total reduction profile can be ascribed to the manganese ions that are in high oxidation states (Mn^{4+}) in each run of catalyst recycling. A downward shift of high-temperature reduction peak [46] indicates that the reducibility of the as-prepared samples followed the trend TO–MCO > MCO>MnO_2 (MO).

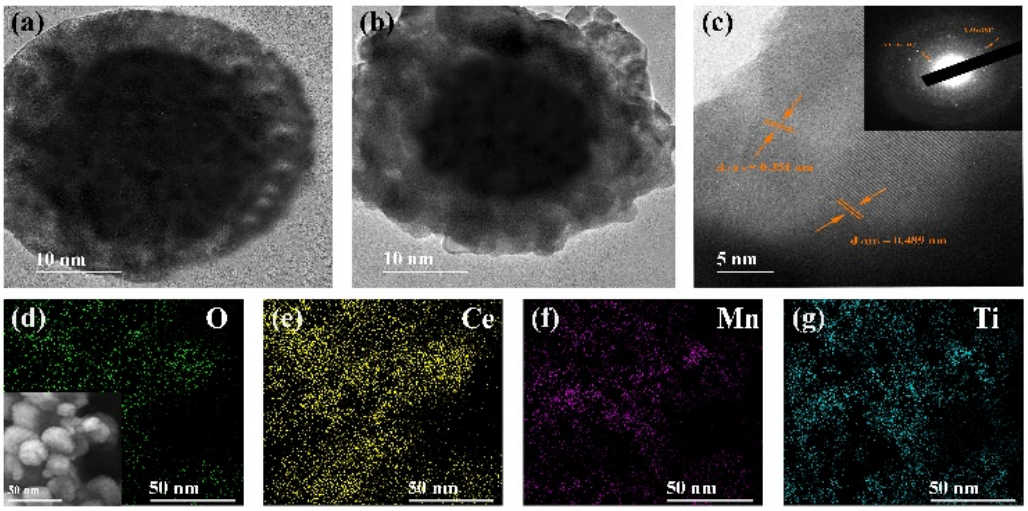

Fig. 2 High-magnification TEM images of MCO (a) and TO–MCO (b); HRTEM images of TO–MCO (c); elemental distribution maps for oxygen, cerium, manganese, and titanium of TO–MCO (d–g).

Scanning electron microscopy (SEM) and transmission electron microscopy (TEM) morphologies were observed in Fig. S4 and Fig. 2, respectively. Compared with micrographs of the as-prepared pristine MnO_2 and CeO_2, the fabrication of the doped Mn^{n+} into CeO_2 considerably modified the surface shape and pore size of MCO, which were composed of highly ordered nanospheres with diameters ranging from 60 nm to 80 nm. The doping treatment of Mn^{n+} with small ionic radius enabled the surface of cubic fluorite-type CeO_2 to obtain an increased porous (111) crystalline property. For TO–MCO, around 5 nm colloidal TiO_2 was deposited on the surface of MCO and showed less effect on the porosity and sphere-like structure of MCO. As expected, the loading treatment enlarged the specific surface area of MCO because its pore size was squeezed and the BET performance of collosol composites was excellent (Table S2). This formation agrees with the presumption that a spherical core is easier to coat with shell-like materials than cuboctahedral or octahedral core shapes. However, the spherical core is often distorted by asymmetric variations in its interface. In other words, few mature techniques can accomplish the extremely similar shape between bimetallic core and shell [46]. The diffraction planes of the MCO and TO–MCO were observed by high-resolution TEM (HRTEM) and the (111) orientation was identified (d111 = 0.489 nm). The TO–MCO sample displayed a distinct lattice plane (101) of TiO_2, with a lattice spacing approximated at 0.351 nm. The (111) lattice plane was observed at the interface between MCO and TiO_2. The transformed crystalline facets that were first detected considerably influenced the TO–MCO catalyst.

3.2. RCD Activity and stability

The increased moistures contributed to the higher HCHO consumption rate and CO_2 production in Fig. 3a and 3b. Unlike the reported transition-metal activity proportionately with rise of temperature [8, 21] and due to extremely volatile sub-ppm HCHO, the opposite effects on the rate show that it reduced dramatically from 45 °C after reaching its maximum at 35 °C in a humid air for TO–MCO, also supported in *in situ* C 1s XPS results (Fig. 5b). Interestingly, the rate of TO–MCO per unit of surface areas ranged 1.41–1.75×10^{-4} μmol·g^{-1}·m^{-2} (RH = 0.7–90 %)

at 35 °C, which were higher than the reported transition metal oxide-based catalysts at low temperature.

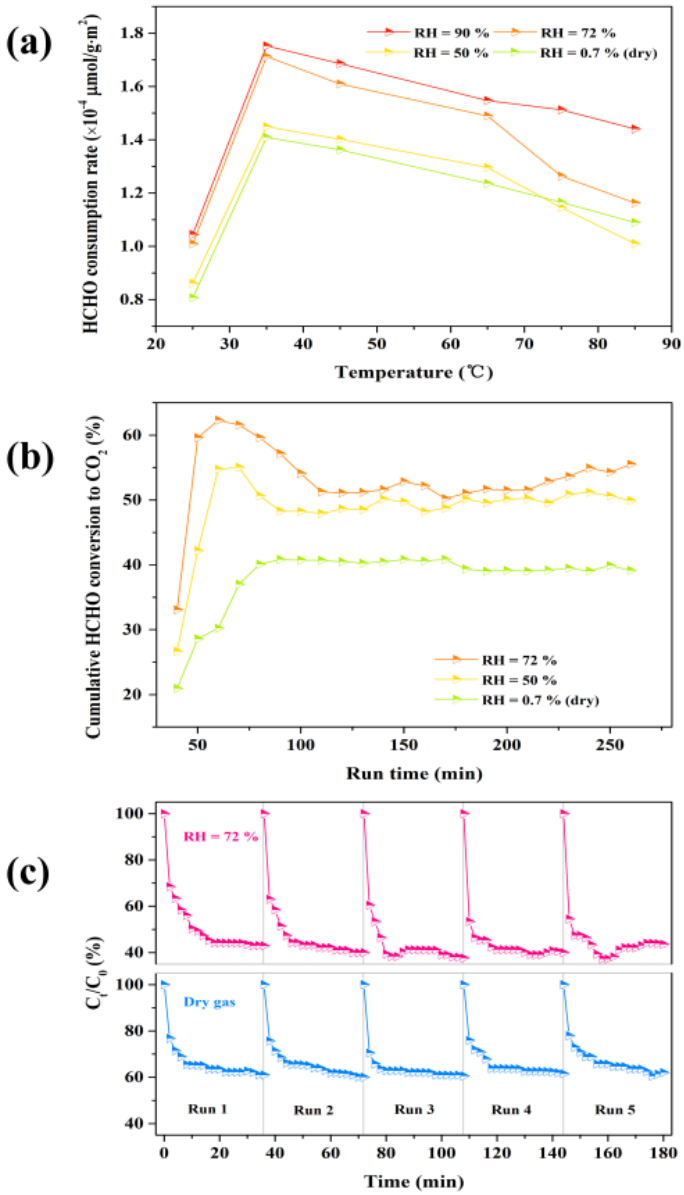

Fig. 3 HCHO consumption rate as a function of reaction temperature over TO–MCO (RH = 0.7–90 %, GHSV =12,000 h^{-1}) (a); cumulative HCHO conversion to CO_2 by TO–MCO (b); recycling catalytic activity by TO–MCO within 3 h (GHSV =12,000 h^{-1}, 35 °C) (c).

In Fig. 3b, the cumulative HCHO conversion to CO_2 over TO–MCO remained 52.4±1.6 % after 120 min in a humid air (RH = 72 %), while it decreased to 39.8±0.8 % in a dry air (RH = 0.7 %). By contrast, the cumulative conversion over MCO dramatically dropped from 40.7±0.3 % at RH = 72 % to 20.8±0.5 % at RH = 0.7 % (Fig. S5). These results proved that TO–MCO outperformed RCD activity at an extensive RH range. Fig. 3c shows the recycling RCD activity by TO–MCO (C_t/C_0 %) in dry and humid airstream at 35 °C within 180 min. The HCHO concentrations decreased rapidly in the first 5 min of each run and finally maintained a stable activity in all 5 recycling runs. TO–MCO leveled off at 57 % with RH of 72 % and 40 % with RH of 0.7 %, ensuing recycling reaction without an obvious decline in activity.

3.3. Probing active-site chemisorption Induced by cyclic electron transfer

The characteristics of the surface electron transfer of the as-prepared catalysts were detected by the voltammogram spectra (Fig. 4). A detailed method on the electrochemical characterization can be found in Text S7. As shown in Fig. 4(a–d), the approximately rectangular shape of cyclic voltammogram was a fingerprint for cycling behavior of charge storage and charge-discharge capacitance [47]. The current density at one certain potential of the as-prepared samples decreased in the following order: TO–MCO > MCO > CeO_2 > MnO_2, which correlated to the distinct composition, high porosity, and large surface specific area. When the scan rate increased, the voltammogram peak and shape of TO–MCO were distorted at higher scan rates as a result of the increase in electron transfer. Compared with its precursors, a more significant shift toward the anodic and cathodic peak positions was ascribed by the presence of the low conductivity oxides for TO–MCO [36, 47], also supported in the observation for electrochemical surface areas (Fig. 4e). Possibly due to the feasibility of crystalline defect in

MCO, the electrochemical surface areas of TO–MCO and MCO were lower than pure CeO_2, which had excellent oxygen storage and capacitance.

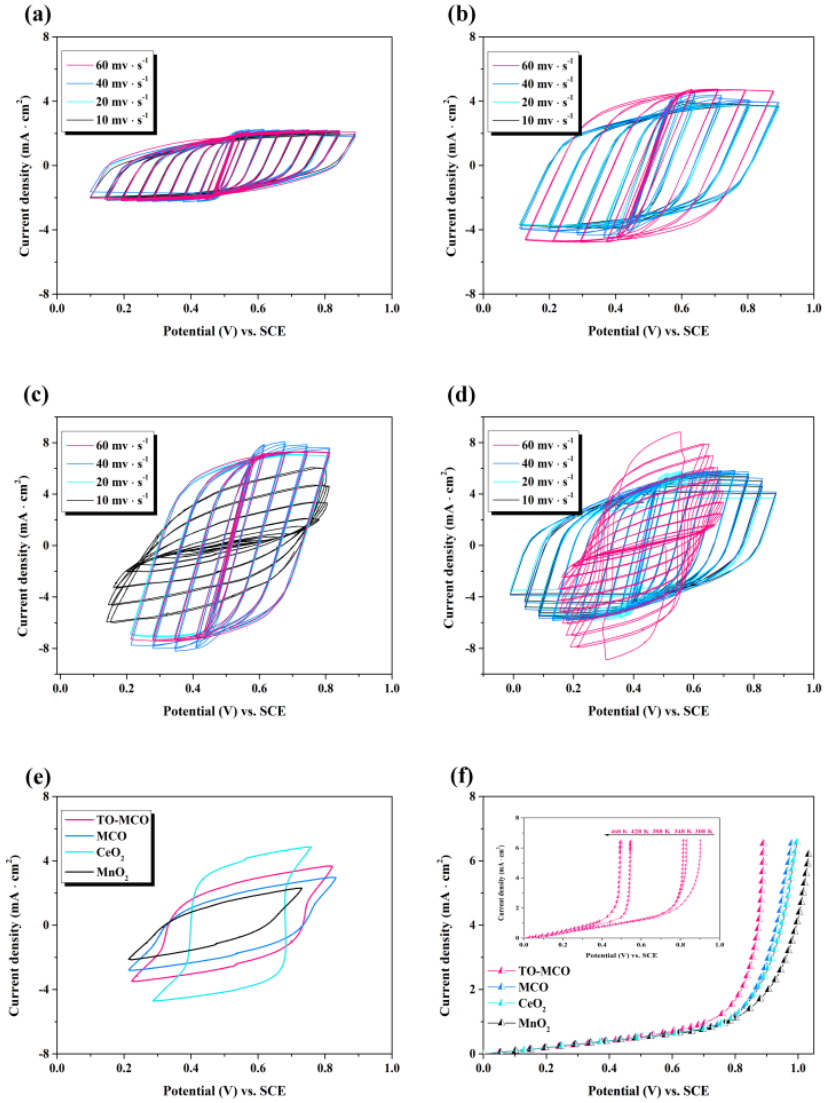

Fig. 4 Cyclic voltammograms at different scan rates in 1 M $Ca(NO_3)_2$ electrolyte (a–c): MnO_2, CeO_2, MCO, and TO–MCO; electrochemical surface area (e); long-term current-potential responses in OER (f) and the responses with increased temperatures for TO–MCO (inset graph of (f)) at a constant scan rate of 10 $mV{\cdot}S^{-1}$ over the range 0–600 s.

Owing to the oxygen-defect (O-defect) remediation, TO–MCO outperformed the capability of active-site enrichment induced by surface electron transfer, which was confirmed by the higher current density with an overpotential close to 1 V for oxygen evolution reaction (OER, Fig. 4f) [32]. As expected, the current-potential responses were largely promoted at increased temperatures (35–195 °C), as shown in the inset graph of Fig. 4f. A suitable adsorption and catalytic activity were actually obtained at decreased temperatures, as shown in Fig. 3 and 5, respectively. The activity was indicated by the extremely high overpotential even though the highest current density was not reached at this temperature. In coordination with the XPS measurements (Fig. S3) and adsorption sites of MnO_x–CeO_2 by density functional theory calculations (Fig. S6, Fig. S7, and Table S3), a large number of free electrons were produced from the cyclic valence transitions of Ce^{4+}–Mn^{3+} ↔ Ce^{3+}–Mn^{4+}. Changes in the oxidized state ratios of Mn^{4+}/Mn and Ce^{3+}/Ce enhanced the participation of oxygen species on the TO–MCO surface throughout the bimetallic dismutation reactions. The perfect MnO_x–CeO_2(111) surfaces (Eads = –2.38 eV) that were remediated by Ti–O depositions on O-defect sites of MnO_x–CeO_2(111) could facilitate to release a better adsorption performance than O-defect surfaces (Eads = –1.58 eV), which also needs to be reexamined and confirmed in future work.

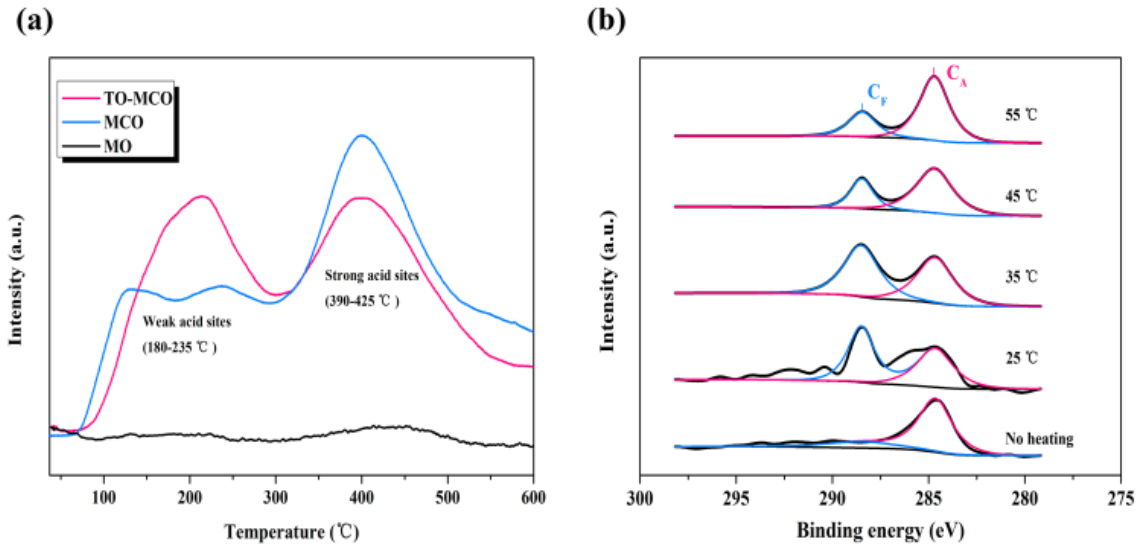

Fig. 5 NH_3–TPD profiles of the as-prepared catalysts (a) and *in situ* C 1s XP spectra of the HCHO-exposed TO–MCO under heating Ar (b).

Room temperatures can counteract the potential of physisorption. Physisorption as an initial preadsorption step that tends to transfer of gaseous pollutants from the gas phase to another phase is still unsatisfactory. Chemisorption starts with physisorption and the strong interaction between the adsorbate and the sorbent surface creates new types of electronic bonds–ionic or covalent. A strong chemical adsorption was ascribed to active-site exposure [48], and high temperatures rather than room temperature enhance catalytic activity in most differential calorimeter reaction catalysts [7, 26, 34]. However, the highly enhanced adsorption and activity of ppb-level HCHO can be successfully achieved at decreased temperature. The acid-base properties are particularly valued for providing an explicit evidence of adsorption strength, number, and distribution of surface active sites [49]. In the NH_3-TPD results (Fig. 5a), two NH_3 desorption peaks were detected. One was in the range of 180–235 °C (weak acid site) and the other at 390–425 °C (strong acid site). CO_2 desorption occurred in a range of 50–250 °C, and OH species started to desorb above 100 °C until they reached their maximum desorption capacity at approximately 200 °C. At 580 °C, nearly all the adsorbed NH_3 completely desorbed or decomposed, and oxygen species already desorbed from the surface at 496 °C [48, 50, 51]. The amount of strong acid sites followed in descending order: MCO > TO–MCO > MnO_2. However, NH_3 was more intensively adsorbed on the TO–MCO surface than on MCO at weak acid sites. Lewis acid sites involving superior selective adsorption of electrolyte cations were presented for polar HCHO molecule, ascribed by the cyclic electron transfer in Fig. 4. Although the strong acid site of MCO exhibited powerful adsorption or reaction with NH_3, TO–MCO performed the active-site exposure and surface porosity in an extensively thermal range at the two kinds of acidic peaks. HCHO adsorption would have gradually deteriorated if the test temperature increased continuously, implying that the enlarged specific surface areas of the TO–MCO catalysts cannot completely recover the adsorption abilities if the active sites are still incompletely exposed [52].

As shown in Fig. 5b, the C 1s signal evolution for the HCHO-exposed TO–MCO was detected via *in situ* C 1s XPS studies at increased temperatures. Herein, the photopeak at lower BE (284.5 eV) was assigned to adventitious carbon (C_A), while the photopeak at 288.5 eV was attributed to the presence of monodendate formate species and/or HCHO (C_F) species bonded end-on through the oxygen atom [18]. Ranging from 25–55 °C, the comparatively strong intensity of the C_F photopeak appeared at 35 °C throughout heating. A gradual decrease in the C_F intensity with increasing temperature was observed, although the proportionate increase in the C_A photopeak was more intense than that in the C_F at the end of this temperature range. Gaseous CO and/or CO_2, as final products of HCHO oxidation, are usually produced at 125–175 °C [18, 53]. However, the conversion of HCHO and/or monodendate formate species can be performed well at room temperature, which was confirmed by the following *in situ* DRIFT measurements.

3.4. Mechanisms for bond cleavage of HCHO

As presented in Fig. 6, no signal of oxygen radicals were detected by ESR methods [54] for pristine MnO_2. However, the four characteristic peaks of 5,5–dimethyl–1–pyrroline N–oxide (DMPO)–$\bullet O_2^-$ at an intensity ratio of approximately 1:1:1:1 were entirely observed after 2 min of irradiation for MCO and TO–MCO. The colloidal TiO_2-supported modification considerably enhanced the activation of $\bullet O_2^-$ compared with MCO. The spectra results were double-checked via radical scavenging experiments [55] (Fig. S8). Since the activated $\bullet O_2^-$ played a substantially greater role in the HCHO decomposition for TO–MCO, the highest catalytic activity was eventually achieved at lower temperature.

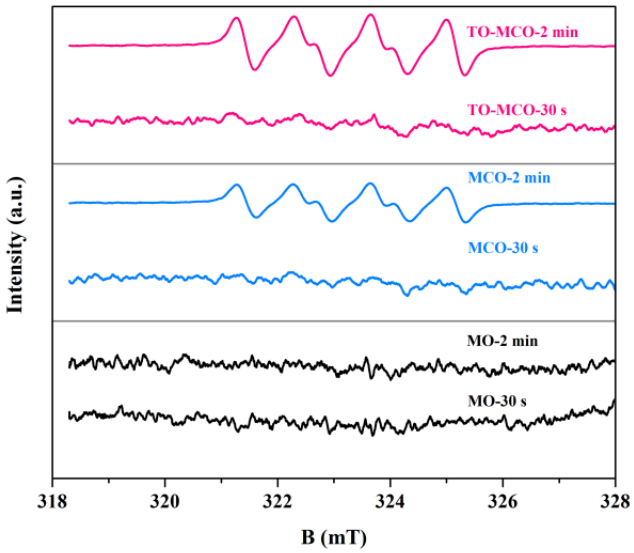

Fig. 6 DMPO spin-trapping ESR spectra at room temperature of ethanol solutions after 30 s and 2 min of irradiation.

To directly determine the possible intermediate species for selective oxidation of HCHO, the high resolution tunable synchrotron photoionization mass spectrometry (detailed measurements are shown in Text S10) was performed. Fig. 7a shows the time-resolved mass spectra over the real-time TO–MCO-exposed HCHO oxidation. The formation of the m/z = 46 species was correlated with the intensity of the CH_2O (m/z = 30) signal. The lifetime signals of CH_2OO and CH_2O were comparatively long but different from that of the CH_2OO species (HCHO oxide from ozonolysis of alkenes) from thermal isomerization or dissociation in atmospheric environment [42]. A faint signal was detected at m/z of 64 and estimated to the generation of hydroxymethyl hydroperoxide ($HOCH_2OOH$, HMHP) possibly from the reaction of CH_2OO with water contents, consistent with the literature estimates [42, 43]. The by-product behavior of $HOCH_2OOH$ is still unknown and seldom investigated in previous studies of HCHO removal. Its production might depend on an increase in water contents. Judging by the differential ionization energies shown in Fig. 7b, the formic acid (10.82 eV) and dioxirane (11.33 eV) that have the identical value of m/z = 46 were recognized (at 298 K and 4 torr) for the assignment of distinct products and matched well with this observation in literature [42, 56]. The intensities in the photoion signals of formic acid and dioxirane varied in different moistures. Clearly, low relative humidity prohibited the adsorption and decomposition of HCHO. The weak dioxirane signal presented a slight change in decay, and one of the –COO single bond species obtained was first detected and established by a comparison with literature estimates [42, 56]. In other words, the refractory dioxirane as one of formate intermediates can exist stably throughout the catalytic oxidation.

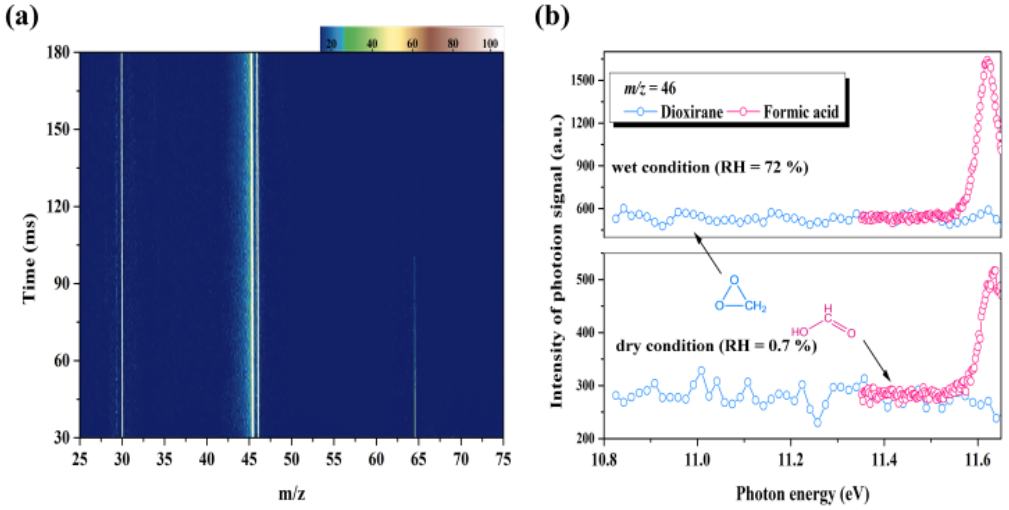

Fig. 7 Time-resolved photoionization mass spectra acquired during exposure of TO–MCO catalysts with CH_2O (a) and photoionization spectra of the *m/z* = 46 products of HCHO decomposition (b). The formation of CH_2OO species were observed at *m/z* = 46 and HCHO (*m/z* = 30) appeared as background.

The formation of intermediate species for HCHO decomposition was recorded via *in situ* DRIFT spectra (Fig. 8). All transient reaction results represented the main formed species that were ascribed to formate species, carbonate, CO_2, and water vapor. The location and shape of absorption peaks were identical for TO–MCO and MCO (Fig. 8a and Fig. S9). But compared with MCO exposure to a dry airstream of

HCHO/21 % O_2/N_2 balance from 25 °C to 85 °C, the absorbance intensity of CO_2 peak (2380 cm^{-1}) and surface hydroxyl species (a remarkable negative peak of 3580 cm^{-1} for υ_s [OH]) increased significantly for TO–MCO. Compared with MCO, TO–MCO at increased temperatures can speed up more conversions of HCHO (1787 cm^{-1}) [7, 21] to carbonate and CO_2, catering for the general property of calorimeter reaction for transition metal oxide-based catalysts. New typical bands indicated the gradual generation of formate species (quite weak 2840 cm^{-1} for υ_s [CH], 1466 cm^{-1} for δ [CH_2], 1562 cm^{-1} for υs [COO], and 1345 and 1314 cm^{-1} for υ_{as} [COO]) [10, 57, 58]. The decomposition of –COO and –CH_2 species resulted from the nucleophilic attack of the reactive oxygen atom. The intensities of –CH_2 and –OH was stronger than that of the –CH match, as indicated by the results of the photoionization mass measurements (Fig. 7). As anticipated, the catalytic performances strongly rely on the effectiveness of rapid decomposition of intermediates. Otherwise, the greater accumulations of −HCOO groups on catalysts, such as the refractory dioxirane which is much more resistant in decomposition than HCHO, would adversely affect the thorough conversion [7].

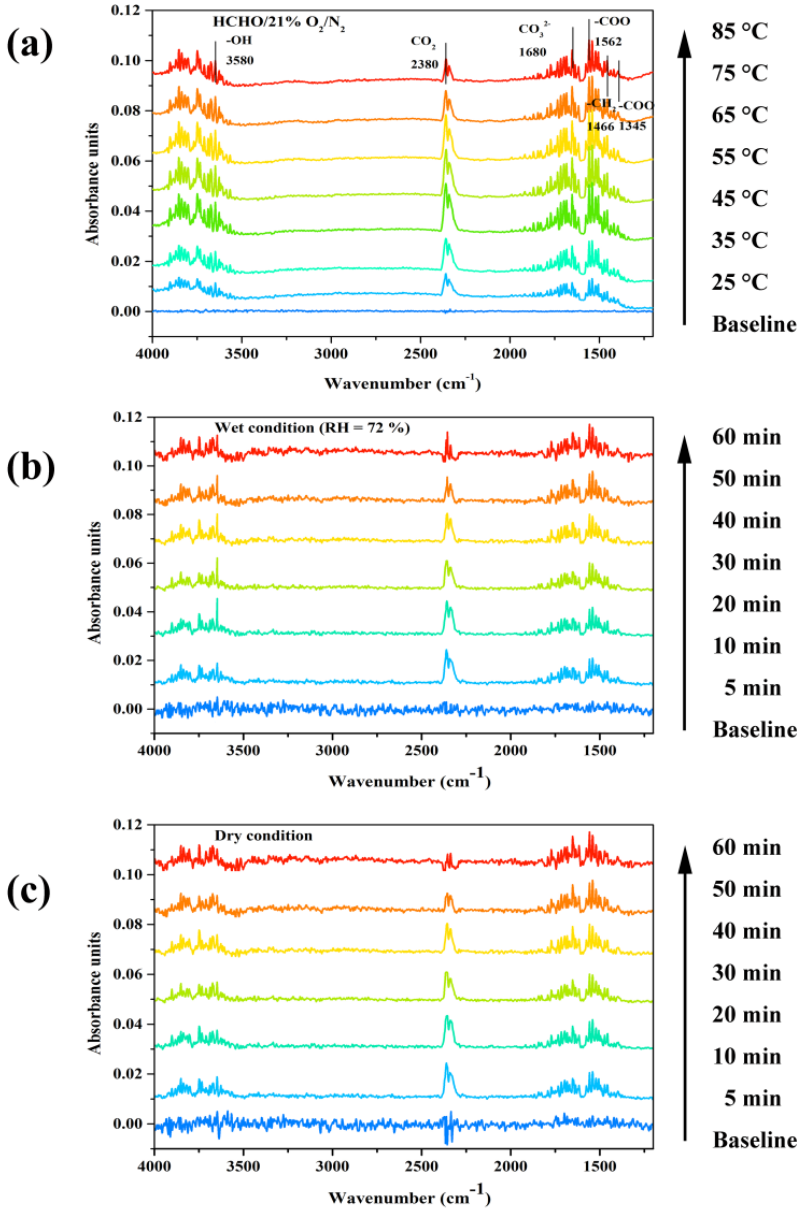

Fig. 8 *In situ* DRIFT spectra of bond cleavage by TO–MCO with increase of react temperature from 25 °C to 85 °C (a); *in situ* DRIFT spectra of bond cleavage by TO–MCO under wet (b) and dry condition (c).

When the temperature reverted to 35 °C for TO–MCO, *in situ* DRIFT spectra in humid air and dry air (Fig. 8b and Fig. 8c) demonstrate that HCHO conversion to formate intermediates can be accelerated in moisture, also confirmed by the photoionization mass spectra in Fig. 7. However, the further conversion of carbonate (1680 cm^{-1}) to CO_2 was weakened with exposure time in dry air, which was possibly ascribed by an interruption of hydrocarbonate pathway [18]. By contrast in dry air, the absorbance peak of CO_2 collected on TO–MCO catalyst reached a higher intensity than that on MCO catalyst at 35 °C (Fig. S9) and was better than the reported transition metal oxide-based catalysts.

$$Mn(IV) + Ce(III) + C^+ \xrightarrow{O_2} Mn(III)/C^+ + Ce(IV)/C^+ + O_2^- + O^- \quad (1)$$

$$Mn(III)/C^{+} + Ce(IV)/C^{+} + e^{-} \rightarrow Mn(IV) + Ce(III) + e^{-} \quad (2)$$

$$O_2^{-} + O^{-} + H_2O + e^{-} \rightarrow \bullet O_2^{-} + 2 - OH, \ (major) \quad (3)$$

$$\bullet O_2^{-} + H^{+} + e^{-} \rightarrow \bullet OH + O^{-}, \ (minor) \quad (4)$$

$$HCHO + C^{+} \xrightarrow{-OH/Ti} HCHO/C^{+} + H_2O \quad (5)$$

$$HCHO/C^{+} + Mn(IV) + \bullet O_2^{-} \rightarrow Mn(III) + HCOO^{-} + -CH_2 \overset{Dioxirane\ (minr)}{_{HMHP\ (faint)}} + H_2O \quad (6)$$

$$HCOO^{-} + -CH_2 + Mn(IV) + \bullet O_2^{-} \rightarrow several\ steps \rightarrow CO_2 + H_2O \quad (7)$$

Apart from the effect of ambient moistures, the reactivity mechanisms of HCHO degradation by TO–MCO at room temperature are proposed as Equations (1–7). In the initial stage, HCHO pre-adsorption was contributed by two dominants. One is the enlarged specific surface area, and the other is chemisorption by cation (represented by 'C^{+}') precipitation on Lewis active sites of the TO–MCO surface. The adsorption and catalytic activity of HCHO were possibly strengthened by interfacial –OH/Ti groups and enhanced by the increased oxidation state of transition-metals. The majority of formate species (i.e., –COO and –CH_2) were mainly decomposed by strong •O_2^{-} activation from the surface chemisorbed oxygen species (O_2^{-} and O^{-}, complex migration species) [8] when capturing the bulk of free electrons (e^{-}) in the bimetallic dismutation reactions. By ensuing nucleophilic attack of •O_2^{-} at –COO double bonds other than •OH, which can be restricted by the consumption of –OH with H^{+} [8, 44], the residual formate species can be further decomposed to produce CO_2 and water vapor as final products.

3.5. Cytotoxity assessment

Before nanoparticles (NPs) release and practical application of the as-prepared catalysts in indoor air purification, their potential adverse effects on the ambient environment and human health must be addressed. Since the cellular structure and organism function of yeast have many similarities with cells in plants and animals [59, 60], the possible cytotoxity of the as-synthesized catalysts was evaluated via the colony-forming units (CFUs) of living cells in the fluorescence cellular scanning microscopy (FCSM with a 488 nm laser for excitation, Olympus laser-based point scanning FV−1000D confocal fluorescent microscope). A methyl thiazolyl tetrazolium (MTT, 0.5 mg·mL^{-1}) assay toward the yeast cells was performed with the colony count method. In the cell viability displayed in Fig. 9, the yeast cells were exposed to NPs which dispersed with different concentrations of 0.5, 5, 10, 25, 50, and 100 μg·mL^{-1} in 5 mM aqueous NaCl solutions. Fig. 9a compared the numbers of CFUs on the yeast-NPs plate with the number of CFUs on the control plate which did not include NPs. The cell viability weakened with the increase in NPs concentration. MCO stimulated the more enhanced proliferation than TO–MCO at above 10 μg·mL^{-1} of NPs concentration but they kept a high value of the yeast cells, over around 80 %.

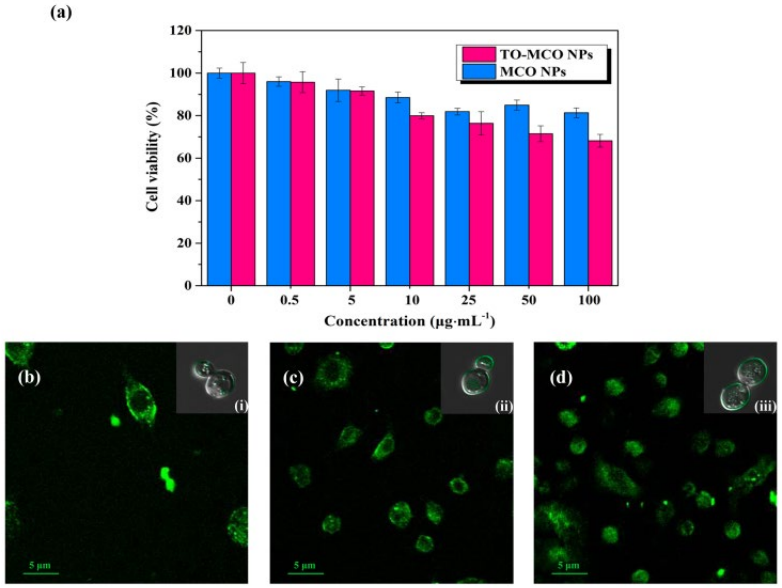

Fig. 9 Viability of yeast cells after incubation of 24-h exposed to different concentrations of the as-synthesized NPs in 5 mM aqueous NaCl solutions (a); Fluorescence cellular scanning images of yeast exposed to 10 μg·mL^{-1} TO–MCO NPs: numbers of CFUs and interference contrast image (i) after 8-h exposure (b), numbers of CFUs and interference contrast image (ii) after 16-h exposure (c), numbers of CFUs and interference contrast image (iii) after 24-h exposure (d).

Considering an exclusion of normal death during the process of cell metabolism, Fig. 9b–d display the time-lapse FCSM images of the yeast cells which were incubated 24-h with 10 μg·mL^{-1} of TO–MCO NPs. The FCSM images of the yeast-NPs visualized a brightly green field and the cells did not appear a significant death throughout exposure to NPs. The bright confocal fluorescent signals were illuminated from

the cell membrane and cytoplasmic area, indicating that the cell membrane was not disrupted and the TO–MCO NPs did not enter into the inner cell nuclei. These observations reveal the benign biocompatibility and low lethal to living organism.

4. Conclusion

The RCD activities of sub-ppm HCHO were first investigated and attributed by the surface active-site exposure and activation of $\bullet O_2^-$ for TO–MCO. The enhanced cyclic electron transfer and hydrophilic self-assembly on TO–MCO particularly compensated the HCHO chemisorption and oxidation in low atmospheric moistures to better than the reported catalysts. The selective oxidation of HCHO follows the pathways from major formic acid, the isomerized dioxirane, and faint $HOCH_2OOH$ into CO_2 and water vapor as final products. While the intensities of these intermediates are strongly associated with water content, the formation and consumption of the refractory dioxirane and $HOCH_2OOH$ are still unclear, which perhaps affect the effectiveness of the thorough HCHO conversion. The benign biocompatibility and low cytotoxity of TO–MCO indicate that it has the promising application in environment cleanup.

Conflicts of interest

There are no conflicts to declare.

Acknowledgements

This research was financially supported by The National Key Research and Development Program of China (2016YFA0203000), The Research Grants Council of Hong Kong Government (PolyU152083/14E and PolyU152090/15E), Hong Kong RGC Collaborative Research Fund (C5022–14G), The Research Grants Council of Hong Kong Government (Project No. T24/504/17), The Ministry of Science and Technology of China (2013FY112700), and partly supported by the National Science Foundation of China (Nos. 41573138). Yu Huang is also supported by the "Hundred Talent Program" of the Chinese Academy of Sciences.

References

1 T. Salthammer, S. Mentese and R. Marutzky, *Chem. Rev.*, 2010, **110**, 2536–2572.
2 A. Luengas, A. Barona, C. Hort, G. Gallastegui, V. Platel and A. Elias, *Rev. Environ. Sci. Bio.*, 2015, **14**, 499–522.
3 Y. Huang, S. S. H. Ho, K. F. Ho, S. C. Lee, J. Z. Yu and P. K. Louie, *J. Hazard. Mater.*, 2011, **186**, 344-351.
4 J. Zhao and X. Yang, *Build. Environ.*, 2003, 38, 645–654.
5 A. H. Mamaghani, F. Haghighat and C. S. Lee, *Appl. Catal. B: Environ.*, 2016, **203**, 247–269.
6 M. Tasbihi, J. K. Bendyna, P. H. Notten and H. T. Hintzen, *J. Nanosci. Nanotechnol.*, 2015, **15**, 6386–6396.
7 L. Nie, J. Yu, M. Jaroniec and F. F. Tao, *Catal. Sci. Technol.*, 2016, **6**, 3649–3669.
8 J. Wang, P. Zhang, J. Li, C. Jiang, R. Yunus and J. Kim, *Environ. Sci. Technol.*, 2015, **49**, 12372–12379.
9 J. Quiroz Torres, S. Royer, J. P. Bellat, J. M. Giraudon and J. F. Lamonier, *ChemSusChem*, 2013, **6**, 578–592.
10 J. Wang, J. Li, C. Jiang, P. Zhou, P. Zhang and J. Yu, *Appl. Catal. B: Environ.*, 2017, **204**, 147–155.
11 M. Li, Z. Zhao, T. Cheng, A. Fortunelli, C. Y. Chen, R. Yu, Q. Zhang, L. Gu, B. Merinov and Z. Lin, *Science*, 2016, **354**, 1414–1419.
12 M. Grzelczak, J. Pérez-Juste, P. Mulvaney and L. M. Liz-Marzán, *Chem. Soc. Rev.*, 2008, **37**, 1783–1791.
13 Q. Xu, W. Lei, X. Li, X. Qi, J. Yu, G. Liu, J. Wang and P. Zhang, *Environ. Sci. Technol.*, 2014, **48**, 9702–9708.
14 M. Lei, D. Wang, J. Li, B. Bai, L. Fu and Y. Li, *Appl. Catal. B: Environ.*, 2014, **148–149**, 36–43.
15 S. Huang, X. Zhu, B. Cheng, J. Yu and C. Jiang, *Environ. Sci*: *Nano*, 2017, **4**, 2215–2224.
16 C. Zhang, Y. Li, Y. Wang and H. He, *Environ. Sci. Technol.*, 2014, **48**, 5816–5822.
17 K. Fujiwara, K. Okuyama and S. E. Pratsinis, *Environ. Sci*: *Nano*, 2017, **4**, 2076–2092.
18 J. Quiroz, J. M. Giraudon, A. Gervasini, C. Dujardin, C. Lancelot, M. Trentesaux and J. F. Lamonier, *ACS Catal.*, 2015, **5**, 2260–2266.
19 P. Yang, J. Li and S. Zuo, *Chem. Eng. Sci.*, 2017, **162**, 218–226.
20 L. Li, F. Jing, J. Yan, J. Jing and W. Chu, *Catal. Today*, 2017, **297**, 167–172.
21 W. Yu, X. Zhu, M. Crocker, B. Chen and C. Shi, *Appl. Catal. B: Environ.*, 2014, **160–161**, 542–551.
22 Y. Wang, A. Zhu, B. Chen, M. Crocker and C. Shi, *Catal. Commun.*, 2013, **36**, 52–57.
23 P. Liu, H. He, G. Wei, X. Liang, F. Qi, F. Tan, T. Wei, J. Zhu and R. Zhu, *Appl. Catal. B: Environ.*, 2015, **182**, 476–484.
24 L. Yan, Y. Liu, K. Zha, H. Li, L. Shi and D. Zhang, *ACS Appl. Mater. Inter.*, 2017, **9**, 2581–2593.
25 R. Gao, D. Zhang, P. Maitarad, L. Shi, T. Rungrotmongkol, H. Li, J. Zhang and W. Cao, *J. Phys. Chem. C*, 2013, **117**, 10502–10511.
26 H. Hu, K. Zha, H. Li, L. Shi and D. Zhang, *Appl. Surf. Sci.*, 2016, **387**, 921–928.
27 M. P. Sang, S. W. Jeon and H. K. Sang, *Catal. Lett.*, 2014, **144**, 756–766.
28 S. Mo, S. Li, J. Li, S. Peng, J. Chen and Y. Chen, *Catal. Commun.*, 2016, **87**, 102–105.
29 E. Saputra, S. Muhammad, H. Sun, H. M. Ang, M. O. Tade and S. Wang, *Environ. Sci. Technol.*, 2013, **47**, 5882–5887.
30 J. Zhang, Y. Li, L. Wang, C. Zhang and H. He, *Catal. Sci. Technol.* , 2015, **5**, 2305–2313.

31 H. Xu, N. Yan, Z. Qu, W. Liu, J. Mei, W. Huang and S. Zhao, *Environ. Sci. Technol.*, 2017, **51**, 8879–8892.
32 Y. Meng, W. Song, H. Huang, Z. Ren, S.-Y. Chen and S. L. Suib, *J. Am. Chem. Soc.*, 2014, **136**, 11452–11464.
33 S. Putla, M. H. Amin, B. M. Reddy, A. Nafady, K. A. A. Farhan and S. K. Bhargava, *ACS Appl. Mater. Inter.*, 2015, **7**, 16525–16535.
34 D. Liu, W. Zhou and J. Wu, *Chem. Eng. J.*, 2016, **284**, 862-871.
35 K. Zha, S. Cai, H. Hu, H. Li, T. Yan, L. Shi and D. Zhang, *J. Phys. Chem. C*, 2017, **121**, 25243–25254.
36 X. Zheng, Z. Han, W. Yang, F. Qu, B. Liu and X. Wu, *Dalton Trans.*, 2016, **45**, 16850–16858.
37 S. Zhang, Q. Fan, H. Gao, Y. Huang, X. Liu, J. Li, X. Xu and X. Wang, *J. Mater. Chem. A*, 2016, **4**, 1414–1422.
38 Y. Wang, C. X. Guo, J. Liu, T. Chen, H. Yang and C. M. Li, *Dalton Trans.*, 2011, **40**, 6388–6391.
39 L. Zhang, D. Zhang, J. Zhang, S. Cai, C. Fang, L. Huang, H. Li, R. Gao and L. Shi, *Nanoscale*, 2013, **5**, 9821–9829.
40 H. Hussain, G. Tocci, T. Woolcot, X. Torrelles, C. L. Pang, D. S. Humphrey, C. M. Yim, D. C. Grinter, G. Cabailh, O. Bikondoa, R. Lindsay, J. Zegenhagen, A. Michaelides and G. Thornton, *Nat. Mater.*, 2017, **16**, 461–466.
41 S. Banerjee, D. D. Dionysiou and S. C. Pillai, *Appl. Catal. B: Environ.*, 2015, **176**, 396–428.
42 O. Welz, J. D. Savee, D. L. Osborn, S. S. Vasu, C. J. Percival, D. E. Shallcross and C. A. Taatjes, *Science*, 2012, **335**, 204–207.
43 W. Chao, J.-T. Hsieh and C.-H. Chang, *Science*, 2015, **347**, 751–754.
44 W. K. Dong, P. W. Seo, G. J. Kim and S. C. Hong, *Appl. Catal. B: Environ.*, 2015, **163**, 436–443.
45 X. Tang, J. Chen, X. Huang, Y. Xu and W. Shen, *Appl. Catal. B: Environ.*, 2008, **81**, 115-121.
46 H. Tan, J. Wang, S. Yu and K. Zhou, *Environ. Sci. Technol.*, 2015, **49**, 8675–8682.
47 Y. Munaiah, B. G. S. Raj, T. P. Kumar and P. Ragupathy, *J. Mater. Chem. A*, 2013, **1**, 4300–4306.
48 P. Kalita, N. M. Gupta and R. Kumar, *J. Catal.*, 2007, **245**, 338–347.
49 T. Saison, N. Chemin, C. Chanéac, O. Durupthy, V. Ruaux, L. Mariey, F. o. Maugé, P. Beaunier and J.-P. Jolivet, *J. Phys. Chem. C*, 2011, **115**, 5657–5666.
50 M. Stanciulescu, P. Bulsink, G. Caravaggio, L. Nossova and R. Burich, *Appl. Surf. Sci.*, 2014, **300**, 201–207.
51 R. Liu, X. Niu, X. Xia, Z. Zeng, G. Zhang and Y. Lu, *RSC Adv.*, 2015, **5**, 62394–62401.
52 P. Deshlahra, R. T. Carr, S. H. Chai and E. Iglesia, *ACS Catal.*, 2015, **5**, 666–682.
53 X. Weng, P. Sun, Y. Long, Q. Meng and Z. Wu, *Environ. Sci. Technol.*, 2017, **51**, 8057–8066.
54 Y. Li, Y. Wang, Y. Huang, J. Cao, W. Ho, S. Lee and C. Fan, *RSC Adv.*, 2015, **5**, 99712–99721.
55 Y. Lu, Y. Huang, J. Cao, W. K. Ho, Q. Zhang, D. Zhu and S. C. Lee, *Ind. Eng. Chem. Res.*, 2016, **55**, 10609–10617.
56 M. T. Nguyen, T. L. Nguyen, V. T. Ngan and H. M. T. Nguyen, *Chem. Phys. Lett.*, 2007, **448**, 183–188.
57 L. Qi, B. Cheng, J. Yu and W. Ho, *J. Hazard. Mater.*, 2015, **301**, 522–530.
58 H. Chen, M. Tang, Z. Rui, X. Wang and H. Ji, *Catal.Today*, 2016, **264**, 23–30.
59 T. Nomura, J. Miyazaki, A. Miyamoto, Y. Kuriyama, H. Tokumoto and Y. Konishi, *Environ. Sci. Technol.*, 2013, **47**, 3417–3423.
60 Y. Huang, Y. Liang, Y. Rao, D. Zhu, J.-j. Cao, Z. Shen, W. Ho and S. C. Lee, *Environ. Sci. Technol.*, 2017, **51**, 2924–2933.